



# Enhanced photocatalytic performance of a two-dimensional BiOIO<sub>3</sub>/g-C<sub>3</sub>N<sub>4</sub> heterostructured composite with a Z-scheme configuration

Yan Gong, Xie Quan\*, Hongtao Yu, Shuo Chen, Huimin Zhao

Key Laboratory of Industrial Ecology and Environmental Engineering (Ministry of Education, China), School of Environmental Science and Technology, Dalian University of Technology, Dalian 116024, China

## ARTICLE INFO

### Keywords:

Photocatalysis  
g-C<sub>3</sub>N<sub>4</sub>  
Layered heterojunction  
Z-scheme

## ABSTRACT

The construction of efficient photocatalytic systems has received considerable attention in the fields of water splitting and environmental remediation because of the great potential of these systems to solve the current energy-related and environmental problems. Herein, a two-dimensional BiOIO<sub>3</sub>/graphitic carbon nitride (g-C<sub>3</sub>N<sub>4</sub>) heterostructured composite bearing BiOIO<sub>3</sub> nanoplates coupled with g-C<sub>3</sub>N<sub>4</sub> nanosheets has been fabricated through a facile electrostatic self-assembly method. The as-prepared hybrids exhibit significantly improved photocatalytic activities toward 2,4,6-trichlorophenol (2,4,6-TCP) degradation and hydrogen evolution in water splitting under simulated solar light irradiation over those of bare g-C<sub>3</sub>N<sub>4</sub>. The apparent rate constant, *k*, for 2,4,6-TCP degradation (0.97 h<sup>−1</sup>) and the hydrogen evolution rate (56.4 μmol h<sup>−1</sup>) of the BiOIO<sub>3</sub>/g-C<sub>3</sub>N<sub>4</sub> composites are approximately 4.8 and 3.5 times higher, respectively, than those of g-C<sub>3</sub>N<sub>4</sub>. The outstanding activity of the hybrids arises from the Z-scheme charge transfer mode, which imparts a superior photogenerated carrier separation ability and strong redox capability. In this Z-scheme, the I<sub>3</sub><sup>−</sup>/I<sup>−</sup> redox pairs formed at the contact interface between BiOIO<sub>3</sub> and g-C<sub>3</sub>N<sub>4</sub> act as electron mediators. This work provides insight into the rational design of other two-dimensional Z-scheme composites with applications in solar energy conversion and environmental remediation.

## 1. Introduction

Photocatalysis utilizing the abundant solar energy to produce a renewable energy source and to perform environmental remediation has been regarded as a promising method for solving the energy shortage crisis and global environmental problems [1–4]. Compared with photocatalysts consisting of a single semiconductor, the development of heterostructured photocatalysts comprising multiple components with tunable band structures and efficient charge carrier separation abilities is considered a promising strategy for achieving highly efficient photocatalytic activity [5]. In particular, Z-scheme hybrid photocatalysts have been gaining immense attention because of the excellent separation capability of the photogenerated charge carriers as well as the preservation of the strong redox ability in the photocatalytic system. To date, several Z-scheme composites with different structures and high photocatalytic performance have been reported [6–10]. Among the composites, two-dimensional (2D) heterostructures are regarded as the most ideal combination due to the significant advantages associated with the abundant coupling interfaces and the short charge transfer distance for efficient photogenerated charge carrier separation [11,12].

Despite the substantial effort that has been devoted to exploring Z-scheme photocatalytic systems, designing a 2D Z-scheme heterostructure is still challenging due to the difficulty in finding suitable photocatalysts with appropriate bandgaps and surface structures for controlling the synthesis of a 2D Z-scheme hybrid photocatalyst. Therefore, exploring photocatalysts appropriate for constructing 2D heterostructured photocatalysts with a Z-scheme configuration is of great interest.

Recent studies have revealed that graphitic carbon nitride (g-C<sub>3</sub>N<sub>4</sub>) can be used as a photocatalyst in water splitting and environmental purification applications primarily because of its peculiar inherent 2D crystal structure, visible light response ability (band gap ~2.7 eV) and excellent chemical stability [13–18]. The photogenerated electrons in the conduction band (CB) of g-C<sub>3</sub>N<sub>4</sub> (−1.3 V) possess a strong reductive ability that is sufficient for reducing pollutants or for water splitting. However, the weak oxidation capacity (+1.4 V) of the photogenerated holes in the valence band (VB) and high recombination rate of the photogenerated electron-hole pairs limits the photocatalytic efficiency of g-C<sub>3</sub>N<sub>4</sub>. Therefore, substantial efforts have been devoted to improving the photocatalytic activity of g-C<sub>3</sub>N<sub>4</sub> by coupling it to other

\* Corresponding author.

E-mail address: [quanxie@dlut.edu.cn](mailto:quanxie@dlut.edu.cn) (X. Quan).

semiconductors [19–21]. Among these other semiconductors, an Aurivillius phase oxide, BiOIO<sub>3</sub>, which is a bismuth-based semiconductor (band gap ~3.0 eV) with a layered structure, maybe one of the most ideal candidates. Benefitting from an internal polar field and the strong oxidizing ability of the photogenerated holes (VB ~4.08 eV based on theoretical calculations), this semiconductor has shown excellent photocatalytic activity in the degradation of organic pollutants under ultraviolet (UV) light irradiation [22], [23]. BiOIO<sub>3</sub> has a layered structure consisting of (Bi<sub>2</sub>O<sub>2</sub>)<sup>2+</sup> slabs connected with (IO<sub>3</sub>)<sup>-</sup> anions. Furthermore, recent studies have demonstrated that the predominant exposed facet of synthesized BiOIO<sub>3</sub> nanoplates is the {010} facet, which is terminated with (IO<sub>3</sub>)<sup>-</sup> groups [24]. Due to the layered features of g-C<sub>3</sub>N<sub>4</sub> and BiOIO<sub>3</sub>, interaction between g-C<sub>3</sub>N<sub>4</sub> and BiOIO<sub>3</sub> can be expected to occur through bonding between the surface-exposed I or O atoms of BiOIO<sub>3</sub> and the C or N atoms of g-C<sub>3</sub>N<sub>4</sub>. This interaction enables the possibility of a valence state change of the iodide ions.

As we know, the reversible redox couple of IO<sub>3</sub><sup>-</sup>/I<sup>-</sup> or I<sub>3</sub><sup>-</sup>/I<sup>-</sup> has been commonly used as an electron transfer mediator in Z-scheme systems [25–27]. Thus, the valence state change of the iodide ions at the contact interface between g-C<sub>3</sub>N<sub>4</sub> and BiOIO<sub>3</sub> can be reasonably assumed to serve as an electron mediator in charge transfer when the two materials are integrated in a heterostructured composite. In this regard, it is possible to construct a 2D Z-scheme heterostructured composite by coupling g-C<sub>3</sub>N<sub>4</sub> with BiOIO<sub>3</sub>. However, to the best of our knowledge, no systematic studies have examined this novel BiOIO<sub>3</sub>/g-C<sub>3</sub>N<sub>4</sub> layered composite with a Z-scheme structure in the removal of organic pollutants and water splitting.

Herein, we report a facile approach toward the fabrication of a BiOIO<sub>3</sub>/g-C<sub>3</sub>N<sub>4</sub> layered composite via electrostatic attraction between positively charged BiOIO<sub>3</sub> nanoplates and negatively charged g-C<sub>3</sub>N<sub>4</sub>. This hybrid composite offers a broadened optical window for effective light harvesting, a short diffusion distance for excellent charge transport, and a large contact area for efficient interfacial charge separation. As a result, the composite is anticipated to exhibit extremely high photocatalytic activities toward 2,4,6-trichlorophenol degradation and hydrogen evolution from water splitting under simulated solar light irradiation.

## 2. Experimental

### 2.1. Synthesis of g-C<sub>3</sub>N<sub>4</sub>, BiOIO<sub>3</sub> and amine-modified BiOIO<sub>3</sub>

The synthesis of g-C<sub>3</sub>N<sub>4</sub> and the BiOIO<sub>3</sub> nanoplates was completed according to the protocols described in previous reports [21,24]. Amine-modified BiOIO<sub>3</sub> nanoplates were obtained by refluxing BiOIO<sub>3</sub> in anhydrous ethanol with aminopropyl triethoxy silane (APTES). In detail, 0.4 g of BiOIO<sub>3</sub> nanoplates was dispersed in 200 mL of anhydrous ethanol containing 2 mL of APTES under vigorous stirring for 12 h to introduce positively charged amine group onto the surface of the BiOIO<sub>3</sub> nanoplates. Then, the APTES-modified BiOIO<sub>3</sub> nanoplates were dried after washing away any remaining APTES with anhydrous ethanol.

### 2.2. Synthesis of BiOIO<sub>3</sub>/g-C<sub>3</sub>N<sub>4</sub> composites

The BiOIO<sub>3</sub>/g-C<sub>3</sub>N<sub>4</sub> composite was fabricated via a facile electrostatic attraction self-assembly method. Briefly, 0.01 g of the APTES-modified BiOIO<sub>3</sub> nanoplates was thoroughly dispersed in 50 mL of ultrapure water by sonication. At the same time, 0.1 g of g-C<sub>3</sub>N<sub>4</sub> was dispersed in 100 mL of ultrapure water by sonication for 30 min. Then, the APTES-modified BiOIO<sub>3</sub> solution was added dropwise into the above g-C<sub>3</sub>N<sub>4</sub> suspension, which was then stirred for 12 h. Next, the mixture was centrifuged at 8000 rpm, washed with ultrapure water three times and dried at 60 °C. Then, the obtained powders were heated at 200 °C for 2 h under a nitrogen atmosphere to obtain the BiOIO<sub>3</sub>/g-C<sub>3</sub>N<sub>4</sub> (10 wt%) nanocomposite. BiOIO<sub>3</sub>/g-C<sub>3</sub>N<sub>4</sub> samples with different

mass ratios of BiOIO<sub>3</sub> (10 wt%, 20 wt%, 30 wt%, 40 wt%, and 50 wt%) were also prepared by the same method and are denoted 10BC, 20BC, 30BC, 40BC, and 50BC, respectively.

### 2.3. Characterization

The crystal structures and element states of the samples were investigated using an X-ray diffractometer (XRD, EMPYREAN, PANalytical, Netherlands) and an X-ray photoelectron spectrometer (XPS, VGESCALAB250, Thermo Fisher Scientific, USA) with Al-Kα irradiation, respectively. The surface functional groups were detected by a Fourier transform infrared spectrophotometer (FT-IR, VERTEX 70, Bruker) with KBr as the reference sample. The morphologies of the samples were investigated using a field emission scanning electron microscope (SEM, Hitachi Co., Japan S-4800) and a transmission electron microscope (TEM, FEI-Tecna, G<sup>2</sup> F30). UV-vis absorption spectra were measured on a Shimadzu UV-2450 spectrophotometer. The zeta potentials of all samples were recorded on a Zeta PALS instrument with water as the solvent. Electron spin resonance (ESR) signals of spin-trapped paramagnetic species with 5,5-dimethyl-1-pyrroline-N-oxide (DMPO) were recorded on a Bruker A200 spectrometer. The photoelectrochemical measurements were conducted on a CHI660B electrochemical system (Shanghai, China) using a standard three-electrode cell. A Pt wire and a saturated calomel electrode (SCE) were used as the counter electrode and the reference electrode, respectively. The electrolyte was 0.05 M Na<sub>2</sub>SO<sub>4</sub> solution.

### 2.4. Evaluation of the photocatalytic activity of BiOIO<sub>3</sub>/g-C<sub>3</sub>N<sub>4</sub>

The photocatalytic performance of the samples was evaluated in the degradation of 2,4,6-trichlorophenol (2,4,6-TCP) and in photocatalytic hydrogen production. A 500 W Xenon lamp was used as a solar light source. The photocatalytic performance was evaluated in the degradation of 2,4,6-TCP with an initial concentration of 50 mg/L. Before irradiation, the sample was dispersed in 50 mL of a 2,4,6-TCP aqueous solution under magnetic stirring for 1 h in the dark to reach the absorption-desorption equilibrium. After desired time intervals, samples were taken and centrifuged to separate the supernatant from the catalyst for analysis. Capture of the active species was performed by employing t-butanol (TBA), ethylenediamine tetraacetic acid disodium salt (EDTA-2Na) and p-benzoquinone (BQ) as scavengers of hydroxyl radicals, holes and ·O<sub>2</sub><sup>-</sup>, respectively. The experiment of photocatalytic H<sub>2</sub> evolution was conducted in a Pyrex reaction vessel connected to a glass closed gas system by using a 300 W Xenon lamp as light source. The apparent quantum efficiency was calculated by the equation:

$$QE[\%] = \frac{\text{number of reacted electrons}}{\text{number of incident photons}} \times 100 = \frac{\text{number of evolved H}_2 \text{ molecules} \times 2}{\text{number of incident photons}} \times 100$$

## 3. Results and discussion

### 3.1. Characterization of the BiOIO<sub>3</sub>/g-C<sub>3</sub>N<sub>4</sub> composites

The overall synthetic procedure for the BiOIO<sub>3</sub>/g-C<sub>3</sub>N<sub>4</sub> hybrids is illustrated in Fig. 1. First, positively charged BiOIO<sub>3</sub> nanoplates were obtained by refluxing BiOIO<sub>3</sub> in ethanol containing 3-aminopropyltriethoxysilane (APTES), which covered the surface of BiOIO<sub>3</sub> with amine functional groups, as evidenced by the zeta potential analysis (Fig. S1). The amine-functionalized BiOIO<sub>3</sub> nanoplates were dispersed in an aqueous solution of g-C<sub>3</sub>N<sub>4</sub> to achieve a homogeneous suspension under stirring. During this process, the BiOIO<sub>3</sub> nanoplates spontaneously coated the g-C<sub>3</sub>N<sub>4</sub> sheets via an electrostatic self-assembly process.

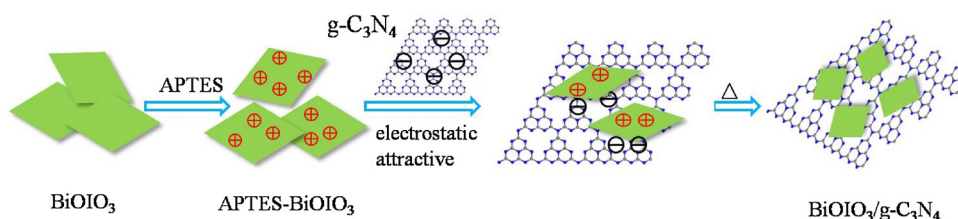


**Fig. 1.** Schematic illustration of the fabrication of  $\text{BiOI/O}_3/\text{g-C}_3\text{N}_4$  composite photocatalyst.

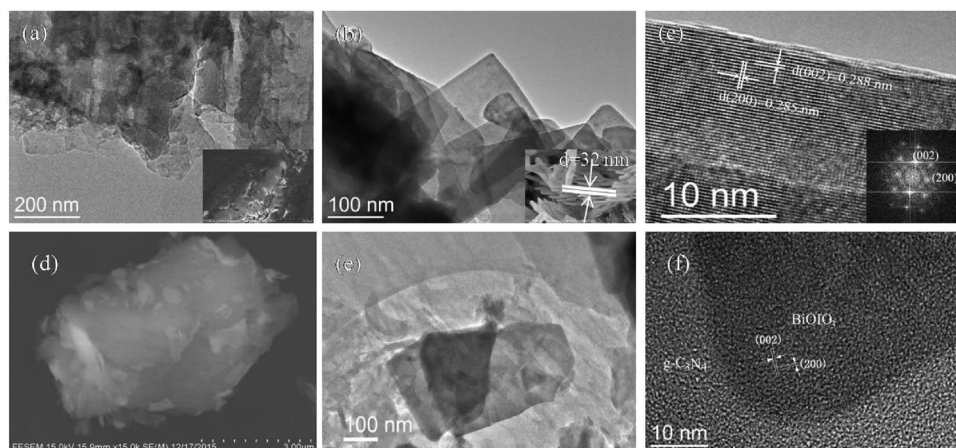


**Fig. 2.** TEM images of (a)  $\text{g-C}_3\text{N}_4$  and (b, c)  $\text{BiOI/O}_3$ ; SEM (d) and TEM images (e, f) of  $\text{BiOI/O}_3/\text{g-C}_3\text{N}_4$ .

TEM images of the two components show that bare  $\text{g-C}_3\text{N}_4$  possesses a sheet-like structure, as displayed in Fig. 2a, and the obtained  $\text{BiOI/O}_3$  material consists of many nanoplates with an average thickness of 20–30 nm (Fig. 2b). The corresponding high-resolution TEM image (Fig. 2c) reveals that the interplanar distances of 0.288 and 0.285 nm can be assigned to the (002) and (200) planes of  $\text{BiOI/O}_3$  [27], and the fast Fourier transform (FFT) patterns (inset of Fig. 2c) also clearly correspond to the [010] zone-axis diffraction spots of orthorhombic  $\text{BiOI/O}_3$ , indicating that the {010} facet is exposed in the synthesized  $\text{BiOI/O}_3$ . From the SEM and TEM images (Fig. 2d–f) of the  $\text{BiOI/O}_3/\text{g-C}_3\text{N}_4$  composite, many nanoplates are clearly horizontally attached to the surface of  $\text{g-C}_3\text{N}_4$  with intimate interfacial contact, confirming the formation of the  $\text{BiOI/O}_3/\text{g-C}_3\text{N}_4$  heterostructure.

Bare  $\text{g-C}_3\text{N}_4$  (Fig. 3a) shows two typical diffraction peaks at  $13.2^\circ$  and  $27.4^\circ$ , corresponding to the (100) and (002) diffraction planes of the  $\text{g-C}_3\text{N}_4$ , respectively [28–34]. All the diffraction peaks of the as-prepared  $\text{BiOI/O}_3$  can be readily indexed to orthorhombic  $\text{BiOI/O}_3$  (ICSD #262019) [23,27]. Only the diffraction peaks assigned to  $\text{BiOI/O}_3$  are observed in the  $\text{BiOI/O}_3/\text{g-C}_3\text{N}_4$  composites, which may be ascribed to the low crystallinity of  $\text{g-C}_3\text{N}_4$  and the overlap between the sharp peaks of  $\text{BiOI/O}_3$  and  $\text{g-C}_3\text{N}_4$  at  $27.4^\circ$ . As shown in the FT-IR spectrum

provided in Fig. 3b, the characteristic peaks corresponding to  $\text{g-C}_3\text{N}_4$  can be observed in all the composites, indicating the presence of the  $\text{g-C}_3\text{N}_4$  phase. In addition, two intense peaks at  $695\text{ cm}^{-1}$  and  $764\text{ cm}^{-1}$ , attributed to the vibration of the I–O bonds in  $\text{BiOI/O}_3$ , can be identified in the hybrids [23,27], which confirm that a hybrid was successfully formed from  $\text{BiOI/O}_3$  and  $\text{g-C}_3\text{N}_4$ .

The Bi 4f (Fig. 4a) and I 2p XPS spectra (Fig. 4b) of the  $\text{BiOI/O}_3/\text{g-C}_3\text{N}_4$  composite indicate the presence of the  $\text{BiOI/O}_3$  phase in the  $\text{BiOI/O}_3/\text{g-C}_3\text{N}_4$  composite [23,27]. Moreover, C 1 s and N 1 s signals are observed in the XPS spectrum of the  $\text{BiOI/O}_3/\text{g-C}_3\text{N}_4$  composite (Fig. 4c and d), confirming the incorporation of the  $\text{g-C}_3\text{N}_4$  phase [28,29,31]. Note that the binding energies of the Bi 4f and I 3d peaks in the composite exhibit a negative shift relative to those of bare  $\text{BiOI/O}_3$ , whereas the N 1 s peaks in the composite show an obvious shift to higher binding energies. This change in the binding energy clearly indicates that electron transfer occurs from  $\text{g-C}_3\text{N}_4$  to  $\text{BiOI/O}_3$ , suggesting strong electronic coupling between  $\text{g-C}_3\text{N}_4$  and  $\text{BiOI/O}_3$ . This coupling may be ascribed to the strong interactions between the  $\text{BiOI/O}_3$  and  $\text{g-C}_3\text{N}_4$  structures that are in close contact, demonstrating the formation of a heterostructure in the  $\text{BiOI/O}_3/\text{g-C}_3\text{N}_4$  composite.

As illustrated in Fig. 5a,  $\text{BiOI/O}_3$  displays a strong adsorption

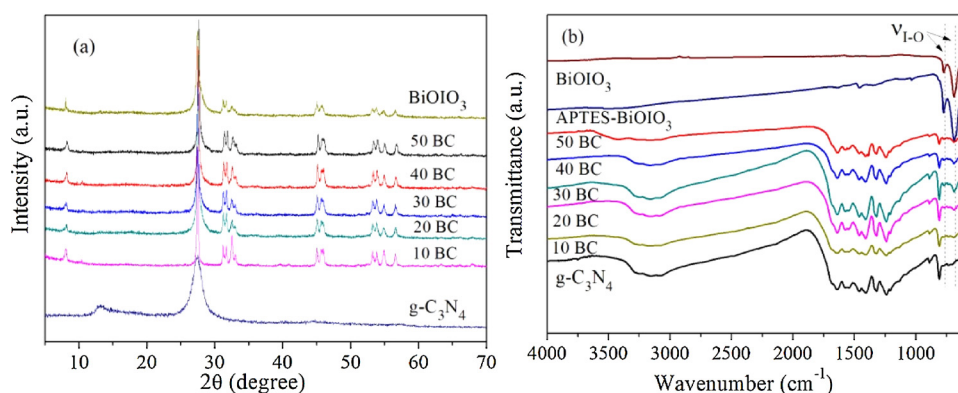


**Fig. 3.** (a) XRD patterns and (b) FTIR spectra of  $\text{g-C}_3\text{N}_4$ ,  $\text{BiOI/O}_3$  and  $\text{BiOI/O}_3/\text{g-C}_3\text{N}_4$ .

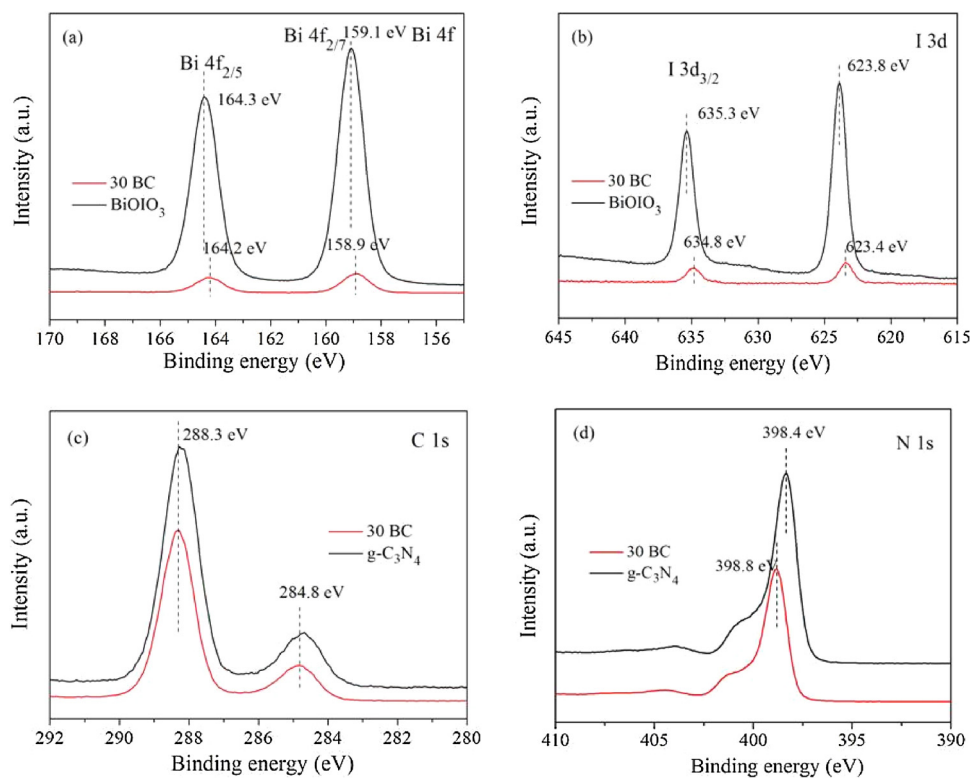


Fig. 4. XPS spectra of the  $\text{BiOIO}_3/\text{g-C}_3\text{N}_4$ : (a, b) the Bi 4f and I 3d of the  $\text{BiOIO}_3$  and  $\text{BiOIO}_3/\text{g-C}_3\text{N}_4$ ; (c, d) the C 1s and N 1s of the  $\text{g-C}_3\text{N}_4$  and  $\text{BiOIO}_3/\text{g-C}_3\text{N}_4$ .

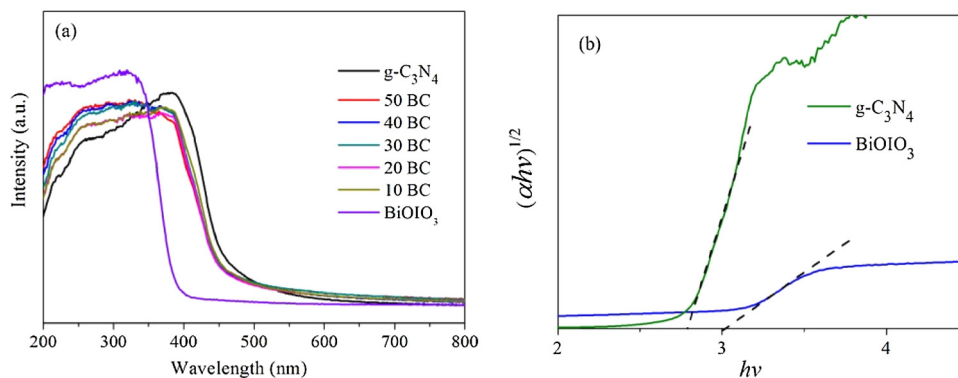


Fig. 5. (a) UV-vis diffuse reflectance spectra of  $\text{g-C}_3\text{N}_4$ ,  $\text{BiOIO}_3$  and  $\text{BiOIO}_3/\text{g-C}_3\text{N}_4$  photocatalysts and (b) the corresponding Tauc plot.

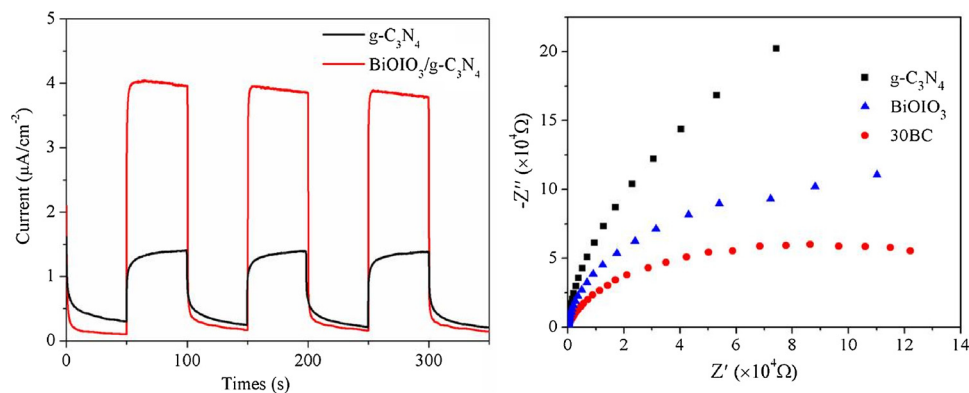
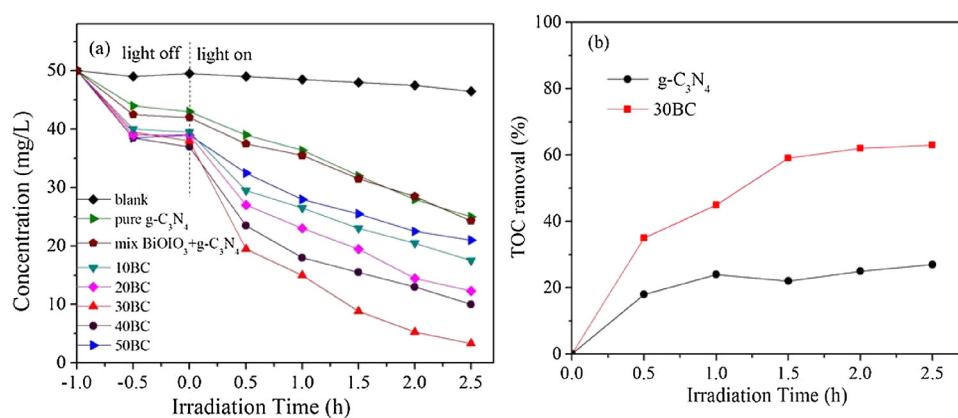
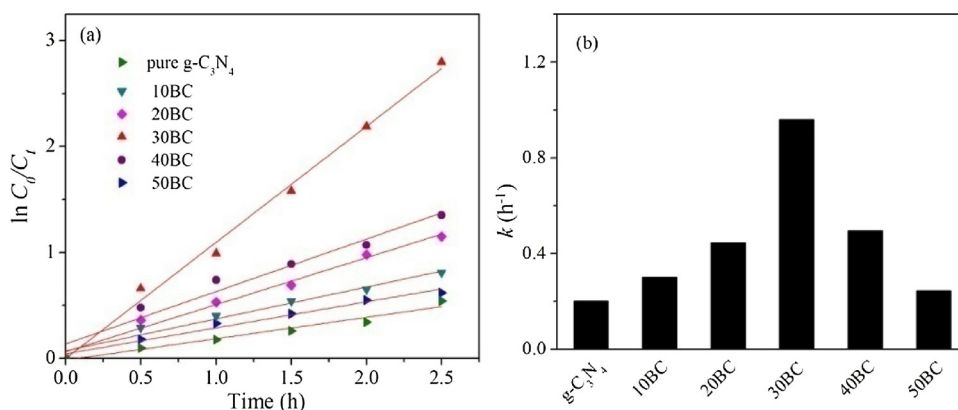


Fig. 6. Transient photocurrent density responses and EIS of  $\text{g-C}_3\text{N}_4$  and  $\text{BiOIO}_3/\text{g-C}_3\text{N}_4$  samples electrodes with light on/off cycles under simulated solar light irradiation.





**Fig. 7.** (a) Photocatalytic activities of g-C<sub>3</sub>N<sub>4</sub> and the BiOI<sub>3</sub>/g-C<sub>3</sub>N<sub>4</sub> composites with different BiOI<sub>3</sub> contents in the degradation of 2,4,6-TCP under simulated solar light irradiation; (b) TOC removal in the degradation of 2,4,6-TCP by g-C<sub>3</sub>N<sub>4</sub> and BiOI<sub>3</sub>/g-C<sub>3</sub>N<sub>4</sub>.



**Fig. 8.** (a) Variation in  $\ln(C_0/C_t)$  with reaction time for 2,4,6-TCP degradation and (b) comparison of the rate constants of 2,4,6-TCP degradation for the different samples.

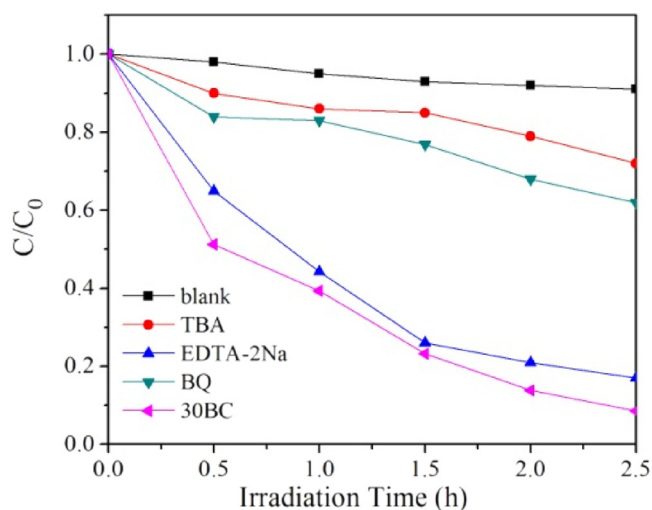


**Fig. 9.** Reactive species trapping experiments of BiOI<sub>3</sub>/g-C<sub>3</sub>N<sub>4</sub> under simulated solar light irradiation.

capability in only the ultraviolet range with an absorption edge at  $\sim 390$  nm, whereas bare g-C<sub>3</sub>N<sub>4</sub> absorbs visible light with wavelengths shorter than 450 nm. The UV–vis spectrum of the BiOI<sub>3</sub>/g-C<sub>3</sub>N<sub>4</sub> composite obtained by loading the BiOI<sub>3</sub> nanoplates onto g-C<sub>3</sub>N<sub>4</sub> reveals that the composite absorbs ultraviolet and visible light. Moreover, the calculated band gaps derived from the Tauc plots (Fig. 5b) of g-C<sub>3</sub>N<sub>4</sub> and BiOI<sub>3</sub> were estimated to be 2.8 eV and 3.0 eV, respectively, which

agree well with the previously reported values [23,28].

Furthermore, the transient photocurrents of g-C<sub>3</sub>N<sub>4</sub> and the as-synthesized BiOI<sub>3</sub>/g-C<sub>3</sub>N<sub>4</sub> composite were measured to investigate the photogenerated electron-hole separation and transfer in the composite [29]. Both g-C<sub>3</sub>N<sub>4</sub> and the as-synthesized BiOI<sub>3</sub>/g-C<sub>3</sub>N<sub>4</sub> composite exhibit rapid and consistent photocurrent responses, as shown in Fig. 6a. Note that the transient photocurrent density of the BiOI<sub>3</sub>/g-C<sub>3</sub>N<sub>4</sub> composite is  $3.8 \mu\text{A cm}^{-2}$ , which is almost 4.1 times higher than that of g-C<sub>3</sub>N<sub>4</sub> ( $0.92 \mu\text{A cm}^{-2}$ ) under solar light irradiation. The enhanced transient photocurrent density of the composite indicates that the separation efficiency of the photogenerated electron-hole pairs in the composite is higher than that in g-C<sub>3</sub>N<sub>4</sub>. The EIS spectra provided in Fig. 6b further support the fast transfer of the photogenerated carriers. This property can be ascribed to the unique geometry of the layered heterostructure of BiOI<sub>3</sub> and g-C<sub>3</sub>N<sub>4</sub>, which shortens the transfer distance of the photogenerated carriers to the reaction sites.

### 3.2. Photocatalytic activity

The photocatalytic activities of g-C<sub>3</sub>N<sub>4</sub> and the BiOI<sub>3</sub>/g-C<sub>3</sub>N<sub>4</sub> composites toward 2,4,6-TCP degradation were evaluated under simulated solar light irradiation. As depicted in Fig. 7a, the blank experiment (without catalyst) demonstrates that 2,4,6-TCP undergoes negligible photodecomposition under solar light irradiation. Prior to the photocatalytic reaction, adsorption experiments with 2,4,6-TCP were performed in the dark and revealed that all the BiOI<sub>3</sub>/g-C<sub>3</sub>N<sub>4</sub> composites possess higher adsorption capabilities toward 2,4,6-TCP than g-C<sub>3</sub>N<sub>4</sub>. This difference may be ascribed to the unique features of the layered heterostructure and its larger specific surface area than that

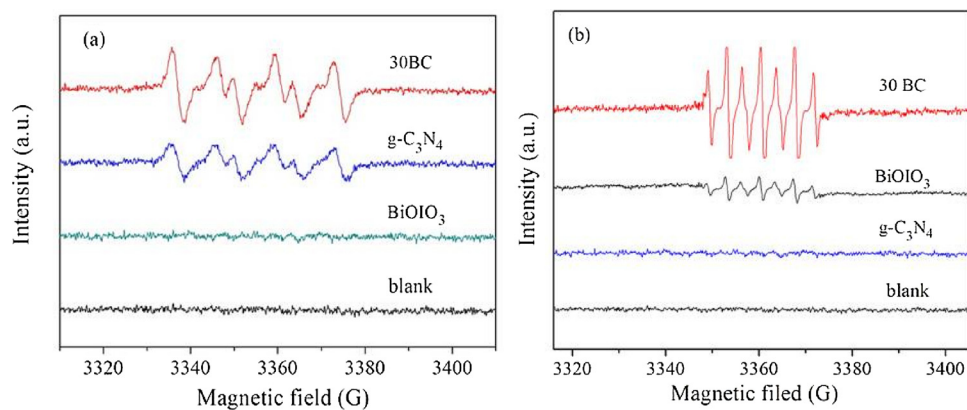


Fig. 10. DMPO spin-trapped ESR spectra of  $\text{g-C}_3\text{N}_4$ ,  $\text{BiOI}_3$  and  $\text{BiOI}_3/\text{g-C}_3\text{N}_4$  (a) in methanol for  $\text{DMPO} \cdot \text{O}_2^-$  and (b) in aqueous solution for  $\text{DMPO} \cdot \text{OH}$ .

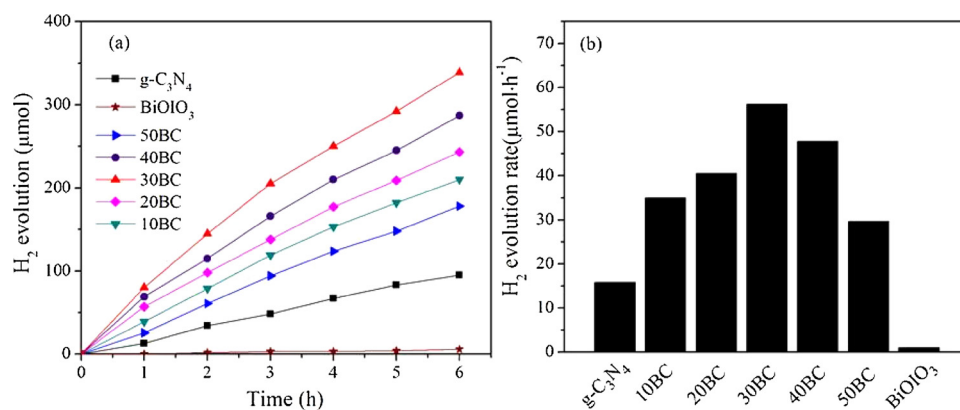


Fig. 11. Photocatalytic  $\text{H}_2$  production by  $\text{g-C}_3\text{N}_4$  and  $\text{BiOI}_3/\text{g-C}_3\text{N}_4$  with different contents of  $\text{BiOI}_3$  under simulated solar light irradiation.

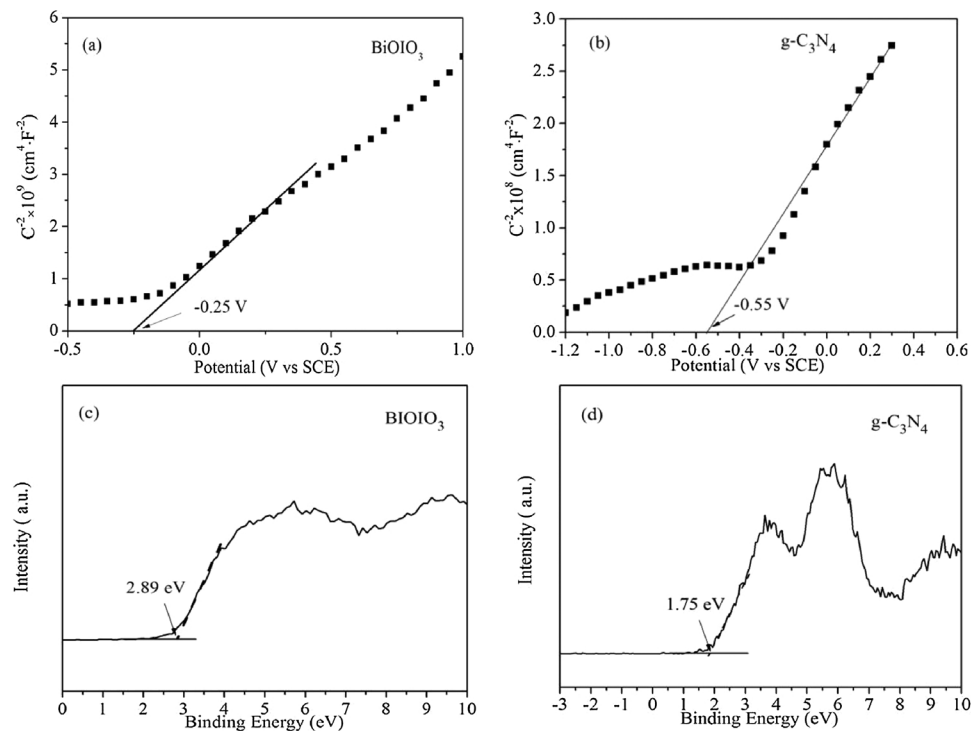


Fig. 12. Mott-Schottky plots of (a)  $\text{BiOI}_3$  and (b)  $\text{g-C}_3\text{N}_4$  and the VB-XPS of (c)  $\text{BiOI}_3$  and (d)  $\text{g-C}_3\text{N}_4$ .

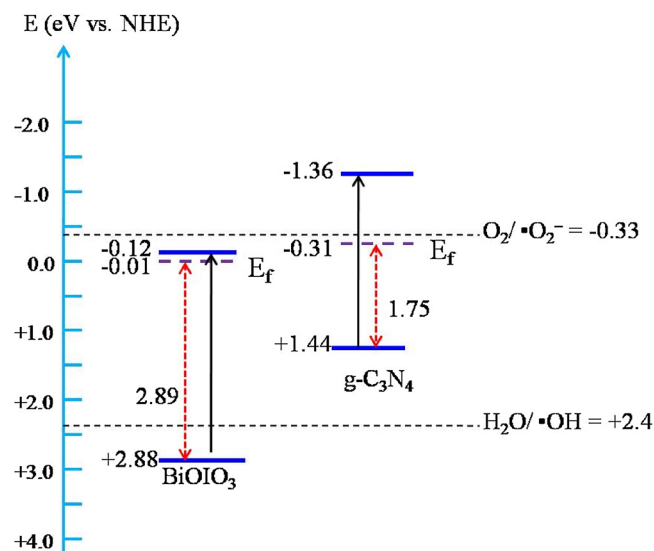


Fig. 13. Schematic diagram of band structure and redox potential of BiOI<sub>3</sub> and g-C<sub>3</sub>N<sub>4</sub>.

of g-C<sub>3</sub>N<sub>4</sub>, which improves the exposure of the active sites for 2,4,6-TCP adsorption. Under simulated solar light irradiation, the BiOI<sub>3</sub>/g-C<sub>3</sub>N<sub>4</sub> composites exhibit remarkably enhanced photocatalytic activity relative to that of g-C<sub>3</sub>N<sub>4</sub> under the same experimental conditions. In particular, the 30% BiOI<sub>3</sub>/g-C<sub>3</sub>N<sub>4</sub> composite (30BC) exhibits the best photocatalytic activity, with a removal ratio of 92% after 2.5 h of irradiation. In addition, the photocatalytic activity of 30BC is higher than that of a physical mixture of BiOI<sub>3</sub> and g-C<sub>3</sub>N<sub>4</sub> (with the same weight ratio of 30 wt%), indicating that the improved photocatalytic activity of the composite can be attributed to the formed heterostructure with intimate interfacial contact between BiOI<sub>3</sub> and g-C<sub>3</sub>N<sub>4</sub>, which boosts the photogenerated charge separation and improves the photocatalytic activity. Also note that the content of BiOI<sub>3</sub> in the composites has a strong influence on the photocatalytic activity of the samples. As the content of BiOI<sub>3</sub> increases from 10% to 30%, the photocatalytic activity of the hybrids is gradually enhanced, and the 30% BiOI<sub>3</sub>/g-C<sub>3</sub>N<sub>4</sub> composite shows the highest photocatalytic activity. However, the photocatalytic activity decreases with the further increase in the BiOI<sub>3</sub> content from 30% to 50%. This subsequent decrease can be explained by the fact that the excess BiOI<sub>3</sub> loaded on the g-C<sub>3</sub>N<sub>4</sub> hinders the light adsorption capability of g-C<sub>3</sub>N<sub>4</sub>, resulting in fewer photogenerated electron-hole pairs in the g-C<sub>3</sub>N<sub>4</sub> that can participate in the reaction. To understand the 2,4,6-TCP degradation kinetics in the presence of different samples, the reaction kinetics of 2,4,6-TCP degradation over g-

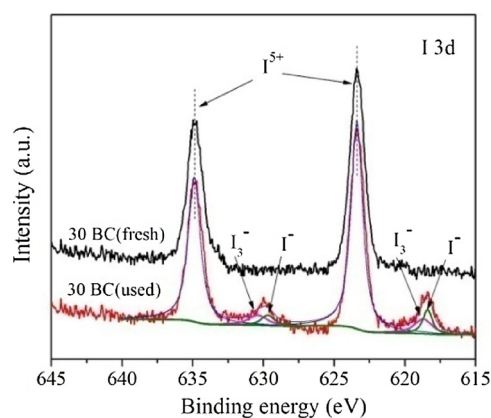


Fig. 15. High-resolution I 3d XPS spectra of the BiOI<sub>3</sub>/g-C<sub>3</sub>N<sub>4</sub> composite before and after the photocatalytic reaction.

C<sub>3</sub>N<sub>4</sub> and the BiOI<sub>3</sub>/g-C<sub>3</sub>N<sub>4</sub> composites were investigated. The linear relationship illustrated in Fig. 8a suggests that the reaction follows pseudo-first-order kinetics. As shown in Fig. 8b, the apparent rate constant, *k*, for 2,4,6-TCP degradation over the 30BC sample is 0.97 h<sup>-1</sup>, which is almost 4.8 times higher than that of bare g-C<sub>3</sub>N<sub>4</sub> (0.21 h<sup>-1</sup>). The total organic carbon (TOC) removal of 2,4,6-TCP in the photocatalytic reaction was measured, and the results are displayed in Fig. 7b. Obviously, the BiOI<sub>3</sub>/g-C<sub>3</sub>N<sub>4</sub> composite (30BC) shows a remarkably high TOC removal (63%) for 2,4,6-TCP degradation after 2.5 h of irradiation, and this removal ratio is higher than that of bare g-C<sub>3</sub>N<sub>4</sub> (only 27%), suggesting the excellent degradation capability of the BiOI<sub>3</sub>/g-C<sub>3</sub>N<sub>4</sub> composite. This result indicates that many more active species can be produced on the BiOI<sub>3</sub>/g-C<sub>3</sub>N<sub>4</sub> composite than on g-C<sub>3</sub>N<sub>4</sub> alone, resulting in the degradation of more 2,4,6-TCP into CO<sub>2</sub> and H<sub>2</sub>O.

Radical trapping experiments were performed to further elucidate the origin of the enhanced photocatalytic activity of the BiOI<sub>3</sub>/g-C<sub>3</sub>N<sub>4</sub> composite (30BC). The effects of adding different scavengers on the efficiency of 2,4,6-TCP degradation are shown in Fig. 9. The efficiency of 2,4,6-TCP degradation decreases markedly after the addition of TBA to the system, which demonstrates that •OH radicals are the predominant active species in the photocatalytic reaction. Meanwhile, the introduction of BQ into the photocatalytic system also decreases the efficiency of 2,4,6-TCP photocatalytic degradation, suggesting that •O<sub>2</sub><sup>-</sup> radicals may also play an important role in the photocatalytic process. In contrast, only a slightly decrease in the efficiency of 2,4,6-TCP degradation is observed when EDTA-2Na is introduced into the photocatalytic system, implying that h<sup>+</sup> has a minor role in the photocatalytic reaction. The above results reveal that •OH and •O<sub>2</sub><sup>-</sup>

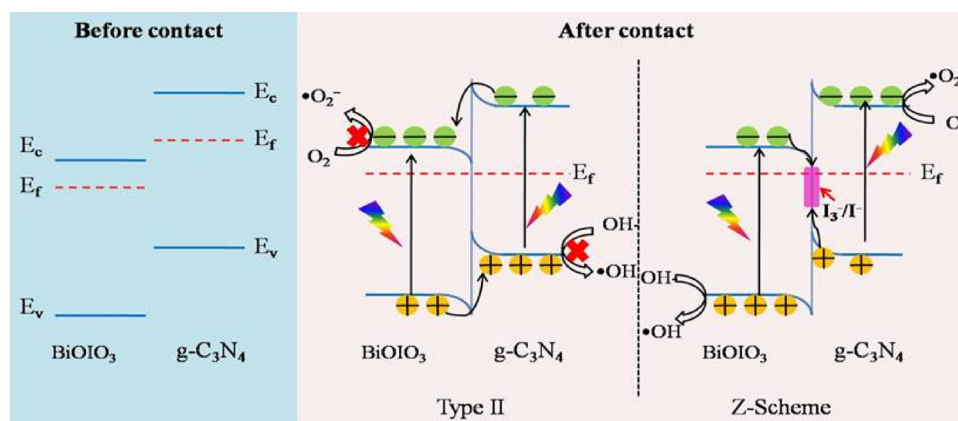


Fig. 14. Schematic diagram of the different transfer pathways of photogenerated carriers in BiOI<sub>3</sub>/g-C<sub>3</sub>N<sub>4</sub>.

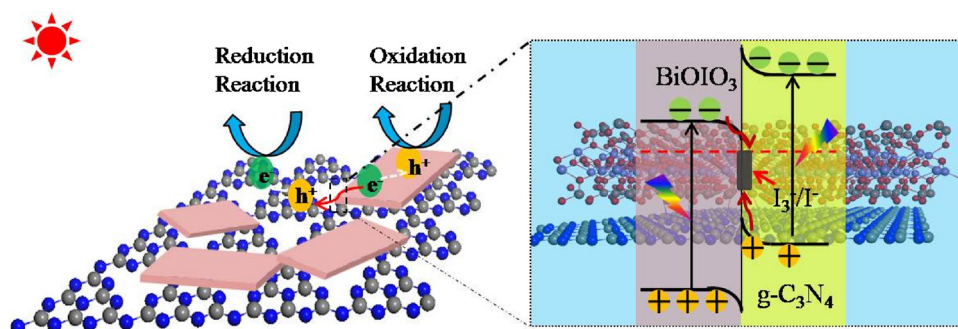


Fig. 16. Mechanism schematic diagram for the photocatalytic reaction over BiOI<sub>3</sub>/g-C<sub>3</sub>N<sub>4</sub> composite under solar light irradiation.

radicals are the primary active species in this photocatalytic system.

To confirm this conclusion, an ESR technique was further employed to detect the active  $\cdot\text{O}_2^-$  radicals in the photocatalytic reaction systems of BiOI<sub>3</sub>, g-C<sub>3</sub>N<sub>4</sub> and the BiOI<sub>3</sub>/g-C<sub>3</sub>N<sub>4</sub> composite under simulated solar light irradiation. As depicted in Fig. 10a, no signals for the DMPO- $\cdot\text{O}_2^-$  adducts can be observed under the blank conditions, which indicates that  $\cdot\text{O}_2^-$  radicals are generated only in the presence of photocatalysts. In the case of bare BiOI<sub>3</sub>, no obvious characteristic peaks of the DMPO- $\cdot\text{O}_2^-$  adducts can be detected, implying that few  $\cdot\text{O}_2^-$  radicals are generated in BiOI<sub>3</sub> reaction system. This result is consistent with those of previous studies [35]. In contrast, the  $\cdot\text{O}_2^-$  signal intensity is obviously stronger for the BiOI<sub>3</sub>/g-C<sub>3</sub>N<sub>4</sub> sample than for g-C<sub>3</sub>N<sub>4</sub>, suggesting that more  $\cdot\text{O}_2^-$  radicals are produced on the BiOI<sub>3</sub>/g-C<sub>3</sub>N<sub>4</sub> surface than on the g-C<sub>3</sub>N<sub>4</sub> surface. Meanwhile, Fig. 10b shows a seven-line spectrum indicating the presence of hydroxyl radicals in the BiOI<sub>3</sub>/g-C<sub>3</sub>N<sub>4</sub> system, which may result from the rapid oxidation of DMPO to DMPOX by two  $\cdot\text{OH}$  radicals generated from the strong oxidation ability of the photogenerated holes in the VB of BiOI<sub>3</sub> [35]. Moreover, fluorescence spectroscopy was employed with terephthalic acid (TA) as a probe to detect the hydroxyl radicals ( $\cdot\text{OH}$ ) in the photocatalytic system, as shown in Fig. S2. The BiOI<sub>3</sub>/g-C<sub>3</sub>N<sub>4</sub> composite shows obviously stronger signal intensities than bare BiOI<sub>3</sub>, indicating that many more hydroxyl radicals can be produced in the BiOI<sub>3</sub>/g-C<sub>3</sub>N<sub>4</sub> composite system than in the system with BiOI<sub>3</sub> alone. Together, the results of the ESR and fluorescence experiments confirmed that large amounts of  $\cdot\text{OH}$  and  $\cdot\text{O}_2^-$  radicals are produced on the surface of the BiOI<sub>3</sub>/g-C<sub>3</sub>N<sub>4</sub> composite.

To gain deeper insight into the photocatalytic reaction process, high-performance liquid chromatography-mass spectrometry (HPLC-MS) was employed to analyze the intermediate products in the photocatalytic degradation of 2,4,6-TCP. As depicted in Figs. S3 and S4, several intermediate product ions are detected at  $m/z$  values of 177.8, 161.7, 143.8 and 113.9 after 1 h irradiation, corresponding to 3,5-dichlorohydroquinone, 2,4-dichlorophenol, 2-chloro-catechol and hydroquinone, respectively. This result suggests that the pathway of photocatalytic 2,4,6-TCP degradation over the BiOI<sub>3</sub>/g-C<sub>3</sub>N<sub>4</sub> composite may follow a dechlorination process. As shown in Fig. S5, the main active species ( $\cdot\text{OH}$  and  $\cdot\text{O}_2^-$  radicals) can attack the chlorine atoms of the benzene ring, causing step-wise decomposition of 2,4,6-TCP to the final CO<sub>2</sub> and H<sub>2</sub>O products. Moreover, the photocatalytic stability of the BiOI<sub>3</sub>/g-C<sub>3</sub>N<sub>4</sub> composite was examined in repeated reactions (Fig. S6), and no appreciable change was observed after 5 cycles (only an 8% decrease in activity), implying that the BiOI<sub>3</sub>/g-C<sub>3</sub>N<sub>4</sub> composite has excellent photostability.

Furthermore, to assess the photocatalytic performance of the BiOI<sub>3</sub>/g-C<sub>3</sub>N<sub>4</sub> heterostructure in the production of renewable energy, a typical H<sub>2</sub> evolution experiment was performed with methanol as a sacrificial agent and Pt (3 wt%) as a cocatalyst under simulated solar light irradiation. As shown in Fig. 11, BiOI<sub>3</sub> showed poor photocatalytic activity toward hydrogen production due to the insufficient reductive ability of the photogenerated electrons. In contrast, g-C<sub>3</sub>N<sub>4</sub>

displayed a hydrogen evolution rate of 15.9  $\mu\text{mol h}^{-1}$ . All the BiOI<sub>3</sub>/g-C<sub>3</sub>N<sub>4</sub> samples exhibited obviously enhanced hydrogen evolution rates compared with that of g-C<sub>3</sub>N<sub>4</sub> alone. The 30% BiOI<sub>3</sub>/g-C<sub>3</sub>N<sub>4</sub> composite (30BC) showed the best photocatalytic activity with a hydrogen evolution rate of 56.4  $\mu\text{mol h}^{-1}$ , which is approximately 3.5 times faster than that of g-C<sub>3</sub>N<sub>4</sub> (15.8  $\mu\text{mol h}^{-1}$ ). The apparent quantum efficiency of 30BC was about 3.9% at 380 nm. This enhanced activity can be attributed to the enhanced charge transfer and separation, which can promote the migration of more photogenerated electrons to the surface to participate in the hydrogen evolution reaction. In addition, the durability of the BiOI<sub>3</sub>/g-C<sub>3</sub>N<sub>4</sub> heterostructure was further evaluated in five consecutive reactions. As shown in Fig. S7, only a slightly decrease ( $\sim 7\%$ ) in the photocatalytic hydrogen evolution activity is observed after five runs, suggesting that the BiOI<sub>3</sub>/g-C<sub>3</sub>N<sub>4</sub> composites have excellent photocatalytic stabilities.

### 3.3. Mechanism of the photocatalytic activity enhancement

The above results clearly reveal that the photocatalytic activity of g-C<sub>3</sub>N<sub>4</sub> can be improved by integrating layered BiOI<sub>3</sub> to form a 2D heterostructure and facilitate charge separation and transport. The band energy alignment of two semiconductors in a heterostructure is known to have an important role in the separation of photogenerated charge carriers. The band edge positions of BiOI<sub>3</sub> and g-C<sub>3</sub>N<sub>4</sub> were evaluated through a combination of Mott-Schottky measurements, valence band X-ray photoelectron spectroscopy (VB-XPS) and UV/Vis spectroscopy [36]. As shown in Fig. 12, the flat-band positions (Fermi energy levels,  $E_f$ ) of BiOI<sub>3</sub> and g-C<sub>3</sub>N<sub>4</sub> obtained from the Mott-Schottky plots are  $-0.25$  and  $-0.55$  V versus the saturated calomel electrode (SCE), respectively, corresponding to  $-0.01$  and  $-0.31$  V versus the normal hydrogen electrode (NHE). The VB XPS results show that the energy gap between the VB and the Fermi level ( $E_{\text{v}f}$ ) is 2.89 eV for BiOI<sub>3</sub> and 1.75 eV for g-C<sub>3</sub>N<sub>4</sub>. Thus, the VB edge potentials of BiOI<sub>3</sub> and g-C<sub>3</sub>N<sub>4</sub> can be calculated and are 2.88 eV and 1.44 eV, respectively. By combining the band gap values derived from Fig. 13, the band energy alignment of BiOI<sub>3</sub>/g-C<sub>3</sub>N<sub>4</sub> can be determined. As illustrated in Fig. S15, the CB and VB positions of BiOI<sub>3</sub> are estimated to be ca.  $-0.12$  eV and 2.88 eV (vs NHE), respectively. Meanwhile, the CB and VB positions of g-C<sub>3</sub>N<sub>4</sub> are located at ca.  $-1.36$  eV and 1.44 eV (vs NHE), respectively. The highly negative potential of the CB in g-C<sub>3</sub>N<sub>4</sub> clearly implies the strong reducing ability of the photogenerated electrons of g-C<sub>3</sub>N<sub>4</sub>, which can reduce adsorbed O<sub>2</sub> to form  $\cdot\text{O}_2^-$  ( $-0.33$  V vs NHE), whereas the photogenerated holes in the VB of g-C<sub>3</sub>N<sub>4</sub> cannot oxidize OH<sup>-</sup> to  $\cdot\text{OH}$  (2.4 V vs NHE) [10,37]. In contrast, BiOI<sub>3</sub> possesses a strong oxidation capability for  $\cdot\text{OH}$  radical formation.

According to energy band theory, the difference between the Fermi levels of BiOI<sub>3</sub> and g-C<sub>3</sub>N<sub>4</sub> causes the electrons in g-C<sub>3</sub>N<sub>4</sub>, which has a higher Fermi level, to flow into BiOI<sub>3</sub> at the interface until the Fermi levels of the two components in the heterostructure are equal, which is consistent with the XPS results. Consequently, the energy band of BiOI<sub>3</sub> bends downward at the contact interface, and that of g-C<sub>3</sub>N<sub>4</sub>



bends upward. As depicted in Fig. 14, two charge transfer pathways are possible in the BiOIO<sub>3</sub>/g-C<sub>3</sub>N<sub>4</sub> heterostructured composite: the traditional route (type II) and the Z-scheme. In the type II route, the photoexcited electrons transfer from the CB of g-C<sub>3</sub>N<sub>4</sub> to the CB of BiOIO<sub>3</sub>; meanwhile, the transfer of photoexcited holes occurs from the VB of BiOIO<sub>3</sub> to the VB of g-C<sub>3</sub>N<sub>4</sub>, resulting in enhanced charge carrier separation. However, the photogenerated holes in the VB of g-C<sub>3</sub>N<sub>4</sub> cannot produce ·OH radicals. Thus, this pathway contradicts the experimental results in which ·OH and ·O<sub>2</sub><sup>−</sup> radicals are the primary active species in the photocatalytic degradation of 2,4,6-TCP over the BiOIO<sub>3</sub>/g-C<sub>3</sub>N<sub>4</sub> composite. Alternatively, according to the above experimental results and analysis, the charge transfer mode in BiOIO<sub>3</sub>/g-C<sub>3</sub>N<sub>4</sub> may follow the Z-scheme, as illustrated in Fig. 14.

Since the electron mediator plays a key role in the charge transfer of the heterostructured composite, the change in the chemical composition of the composite after the photocatalytic reaction was investigated by XPS, as depicted in Fig. 15. Compared with the as-synthesized BiOIO<sub>3</sub>/g-C<sub>3</sub>N<sub>4</sub> composite (30BC), two new peaks corresponding to low-valent iodine ions are observed at 630.4 eV and 618.3 eV in the I 3d XPS spectrum of the sample after the photocatalytic reaction, implying the presence of low-valent iodine ions in the composite. The peaks were deconvoluted into two components, which are assigned to I<sub>3</sub><sup>−</sup> and I<sup>−</sup> ions [28,38], respectively. These low-valent iodine ions may be derived from the interactions between the iodine atoms of BiOIO<sub>3</sub> and the nitrogen atoms of g-C<sub>3</sub>N<sub>4</sub> or the reduction of I<sup>5+</sup> ions at the interfacial defects during the photocatalytic reaction. Thus, these I<sub>3</sub><sup>−</sup>/I<sup>−</sup> redox pairs at the interface between g-C<sub>3</sub>N<sub>4</sub> and BiOIO<sub>3</sub> can be expected to act as electron mediators in the electron transfer from the CB of BiOIO<sub>3</sub> to the VB of g-C<sub>3</sub>N<sub>4</sub>, as illustrated in Fig. 16. The strongly reducing photogenerated electrons remaining in the CB of g-C<sub>3</sub>N<sub>4</sub> can then reduce both O<sub>2</sub> to form ·O<sub>2</sub><sup>−</sup> radicals and H<sup>+</sup> to form H<sub>2</sub>, and the photogenerated holes on the surface of BiOIO<sub>3</sub> can participate in a surface oxidation reaction to produce ·OH radicals; Both of these pathways are consistent with the above experimental results.

In summary, we report the fabrication of a 2D heterostructured BiOIO<sub>3</sub>/g-C<sub>3</sub>N<sub>4</sub> composite via a facile electrostatic self-assembly method. The as-prepared BiOIO<sub>3</sub>/g-C<sub>3</sub>N<sub>4</sub> composite exhibits remarkably enhanced photocatalytic activities toward 2,4,6-TCP degradation and H<sub>2</sub> evolution relative to those of g-C<sub>3</sub>N<sub>4</sub>. The apparent rate constant, *k*, for 2,4,6-TCP degradation and the hydrogen evolution rate over the 30BC sample are 0.97 h<sup>−1</sup> and 56.4 μmol h<sup>−1</sup>, respectively, which are approximately 4.8 and 3.5 times higher than those of g-C<sub>3</sub>N<sub>4</sub>. This improved photocatalytic activity can be attributed to the unique 2D heterostructure, which possesses a large specific surface area and abundant coupling interfaces, as well as the Z-scheme charge transfer mode in which I<sub>3</sub><sup>−</sup>/I<sup>−</sup> redox pairs act as the electron mediator at the interface, giving rise to efficient separation of the photogenerated charge carriers and a strong redox ability for photocatalytic water splitting and removal of organic pollutants. This work provides a strategy for designing other novel 2D composites with enhanced photocatalytic performance in environmental remediation applications or the production of renewable energy sources.

## Acknowledgments

This work was supported by the National Natural Science Foundation of China (21590813) and the Programme of Introducing Talents of Discipline to Universities (B13012).

## Appendix A. Supplementary data

Supplementary material related to this article can be found, in the online version, at doi:<https://doi.org/10.1016/j.apcatb.2018.06.060>.

## References

- [1] A. Kubacka, M. Fernández-García, G. Colón, Advanced nanoarchitectures for solar photocatalytic applications, *Chem. Rev.* 112 (2012) 1555–1614.
- [2] X.B. Chen, S.H. Shen, L.J. Guo, S.Mao Samuel, Semiconductor-based photocatalytic hydrogen generation, *Chem. Rev.* 110 (2010) 6503–6570.
- [3] S.N. Habisreutinger, L. Schmidt-Mende, J.K. Stolarczyk, Photocatalytic reduction of CO<sub>2</sub> on TiO<sub>2</sub> and other semiconductors, *Angew. Chem. Int. Ed.* 52 (2013) 7372–7408.
- [4] H. Tong, S.X. Ouyang, Y.P. Bi, N. Umezawa, M. Oshikiri, J.H. Ye, Nano-photocatalytic materials: possibilities and challenges, *Science* 331 (2011) 746.
- [5] U.I. Gaya, A.H. Abdullah, Heterogeneous photocatalytic degradation of organic contaminants over titanium dioxide: a review of fundamentals, progress and problems, *J. Photochem. Photobiol. C: Photochem. Rev.* 9 (2008) 1–12.
- [6] H. Tada, T. Mitsui, T. Kiyonaga, T. Akita, K. Tanaka, All-solid-state Z-scheme in CdS–Au–TiO<sub>2</sub> three-component nanofunction system, *Nat. Mater.* 5 (2006) 782.
- [7] Y. Sasaki, H. Kato, A. Kudo, Artificial z-scheme constructed with a supramolecular metal complex and semiconductor for the photocatalytic reduction of CO<sub>2</sub>, *J. Am. Chem. Soc.* 135 (2013) 4596–4599.
- [8] H.J. Li, Y.Y. Gao, Y. Zhou, F.T. Fan, Q.T. Han, Q.F. Xu, X.Y. Wang, X.M. Li, C. Z.G. Zou, Construction and nanoscale detection of interfacial charge transfer of elegant Z-scheme WO<sub>3</sub>/Au/In<sub>2</sub>S<sub>3</sub> nanowire arrays, *Nano Lett.* 16 (2016) 5547.
- [9] C. Liu, J. Tang, H.M. Chen, B. Liu, P.D. Yang, A fully integrated nanosystem of semiconductor nanowires for direct solar water splitting, *Nano Lett.* 13 (2013) 2989–2992.
- [10] S.F. Chen, Y.F. Hu, S.G. Meng, X.L. Fu, Study on the separation mechanisms of photogenerated electrons and holes for composite photocatalysts g-C<sub>3</sub>N<sub>4</sub>-WO<sub>3</sub>, *Appl. Catal. B* 150–151 (2014) 564–573.
- [11] X. Huang, C.L. Tan, Z.Y. Yin, H. Zhang, Hybrid nanostructures based on two-dimensional nanomaterials, *Adv. Mater.* 26 (2014) 2185–2204.
- [12] Y. Hou, Z.M. Wen, S.M. Cui, X.R. Guo, J.H. Chen, Constructing 2D porous graphitic C<sub>3</sub>N<sub>4</sub> nanosheets/nitrogen-doped graphene/layered MoS<sub>2</sub> ternary nanofunction with enhanced photoelectrochemical activity, *Adv. Mater.* 25 (2013) 6291–6297.
- [13] X.C. Wang, K. Maeda, A. Thomas, K. Takanabe, G. Xin, J.M. Carlsson, K. Domen, M. Antonietti, Polymer semiconductors for artificial photosynthesis: hydrogen evolution by mesoporous graphitic carbon nitride with visible light, *Nat. Mater.* 8 (2009) 76–80.
- [14] Y. Wang, X.C. Wang, M. Antonietti, Polymeric graphitic carbon nitride as a heterogeneous organocatalyst: from photochemistry to multipurpose catalysis to sustainable chemistry, *Angew. Chem. Int. Ed.* 51 (2012) 68–89.
- [15] J.J. Zhu, P. Xiao, H.L. Li, S.A.C. Carabineiro, Graphitic carbon nitride: synthesis, properties, and applications in catalysis, *ACS Appl. Mater. Interfaces* 6 (2014) 16449–16465.
- [16] X.C. Wang, S. Blechert, M. Antonietti, Polymeric graphitic carbon nitride for heterogeneous photocatalysis, *ACS Catal.* 2 (2012) 1596–1606.
- [17] G.P. Dong, Y.H. Zhang, Q.W. Pan, J.R. Qiu, A fantastic graphitic carbon nitride (g-C<sub>3</sub>N<sub>4</sub>) material: electronic structure, photocatalytic and photoelectronic properties, *J. Photochem. Photobiol. C: Photochem. Rev.* 20 (2014) 33–50.
- [18] W.J. Wang, J.C. Yu, D.H. Xia, P.K. Wong, Y.C. Li, Graphene and g-C<sub>3</sub>N<sub>4</sub> nanosheets wrapped elemental α-Sulfur as a novel metal-free heterojunction photocatalyst for bacterial inactivation under visible-light, *Environ. Sci. Technol.* 48 (2014) 11984–11990.
- [19] Q.J. Xiang, J.G. Yu, M. Jaroniec, Preparation and enhanced visible-light photocatalytic H<sub>2</sub>-production activity of Graphene/C<sub>3</sub>N<sub>4</sub> composites, *J. Phys. Chem. C* 115 (2011) 7355–7363.
- [20] H.F. Shi, G.Q. Chen, C.L. Zhang, Z.G. Zou, Polymeric g-C<sub>3</sub>N<sub>4</sub> coupled with NaNO<sub>3</sub> nanowires toward enhanced photocatalytic reduction of CO<sub>2</sub> into renewable fuel, *ACS Catal.* 4 (2014) 3637–3643.
- [21] Y.Z. Hong, Y.H. Jiang, C.S. Li, W.Q. Fan, X. Yan, M. Yan, W.D. Shi, In-situ synthesis of direct solid-state Z-scheme V<sub>2</sub>O<sub>5</sub>/g-C<sub>3</sub>N<sub>4</sub> heterojunctions with enhanced visible light efficiency in photocatalytic degradation of pollutants, *Appl. Catal. B* 180 (2016) 663–673.
- [22] S.D. Nguyen, J. Yeon, S.-H. Kim, P.S. Halasyamani, BiO(IO<sub>3</sub>): a new polar iodate that exhibits an Aurivillius-type (Bi<sub>2</sub>O<sub>2</sub>)<sup>2+</sup> layer and a large SHG response, *J. Am. Chem. Soc.* 133 (2011) 12422–12425.
- [23] W.J. Wang, B.B. Huang, X.C. Ma, Z.Y. Wang, X.Y. Qin, X.Y. Zhang, Y. Dai, M.-H. Whangbo, Efficient separation of photogenerated electron-hole pairs by the combination of a heterolayered structure and internal polar field in pyroelectric BiOIO<sub>3</sub> nanoplates, *Chem. Eur. J.* 19 (2013) 14777–14780.
- [24] F. Dong, T. Xiong, Y.J. Sun, Y.X. Zhang, Y. Zhou, Controlling interfacial contact and exposed facets for enhancing photocatalysis via 2D–2D heterostructures, *Chem. Commun.* 51 (2015) 8249–8252.
- [25] P. Zhou, J.G. Yu, M. Jaroniec, All-solid-state Z-scheme photocatalytic systems, *Adv. Mater.* 26 (2014) 4920–4935.
- [26] H.J. Li, W.G. Tu, Y. Zhou, Z.G. Zou, Z-scheme photocatalytic systems for promoting photocatalytic performance: recent progress and future challenges, *Adv. Sci.* 3 (2016) 1500389(1–12).
- [27] K. Maeda, M. Higashi, D.L. Lu, R. Abe, K. Domen, Efficient nonsacrificial water splitting through two-step photoexcitation by visible light using a modified oxynitride as a hydrogen evolution photocatalyst, *J. Am. Chem. Soc.* 132 (2010) 5858–5868.
- [28] J.C. Wang, H.C. Yao, Z.Y. Fan, L. Zhang, J.S. Wang, S.Q. Zang, Z.J. Li, Indirect Z-scheme BiOI/g-C<sub>3</sub>N<sub>4</sub> photocatalysts with enhanced photoreduction CO<sub>2</sub> activity under visible light irradiation, *ACS Appl. Mater. Interfaces* 8 (2016) 3765–3775.
- [29] X.J. Bai, L. Wang, Y.J. Wang, W.Q. Yao, Y.F. Zhu, Enhanced oxidation ability of g-

- C<sub>3</sub>N<sub>4</sub> photocatalyst via C<sub>60</sub> modification, *Appl. Catal. B* 152–153 (2014) 262–270.
- [30] H. Wang, Y. Su, H.X. Zhao, H.T. Yu, S. Chen, Y.B. Zhang, X. Quan, Photocatalytic oxidation of aqueous ammonia using atomic single layer graphitic-C<sub>3</sub>N<sub>4</sub>, *Environ. Sci. Technol.* 48 (2014) 11984–11990.
- [31] Y.M. He, L.H. Zhang, B.T. Teng, M.H. Fan, New application of Z-scheme Ag<sub>3</sub>PO<sub>4</sub>/g-C<sub>3</sub>N<sub>4</sub> composite in converting CO<sub>2</sub> to fuel, *Environ. Sci. Technol.* 49 (2015) 649–656.
- [32] Y.X. Li, S.X. Ouyang, H. Xu, X. Wang, Y.P. Bi, Y.F. Zhang, J.H. Ye, Constructing solid–gas-interfacial Fenton reaction over alkalized-C<sub>3</sub>N<sub>4</sub> photocatalyst to achieve apparent quantum yield of 49% at 420 nm, *J. Am. Chem. Soc.* 138 (2016) 13289–13297.
- [33] H.X. Zhao, H.T. Yu, X. Quan, S. Chen, Y.B. Zhang, H.M. Zhao, H. Wang, Fabrication of atomic single layer graphitic-C<sub>3</sub>N<sub>4</sub> and its high performance of photocatalytic disinfection under visible light irradiation, *Appl. Catal. B* 152–153 (2014) 46–50.
- [34] D.M. Chen, K.W. Wang, W.Z. Hong, R.L. Zong, W.Q. Yao, Y.F. Zhu, Visible light photoactivity enhancement via CuTCPP hybridizedg-C<sub>3</sub>N<sub>4</sub> nanocomposite, *Appl. Catal. B* 166–167 (2015) 366–373.
- [35] H.W. Huang, S.C. Tu, C. Zeng, T.R. Zhang, H. Reshak, Ali, Y.H. Zhang, Macroscopic polarization enhancement promoting photo- and piezoelectric-induced charge separation and molecular oxygen activation, *Angew. Chem. Int. Ed.* 56 (2017) 11860–11864.
- [36] H.F. Li, H.T. Yu, X. Quan, S. Chen, H.M. Zhao, Improved photocatalytic performance of heterojunction by controlling the contact facet: high electron transfer capacity between TiO<sub>2</sub> and the {110} facet of BiVO<sub>4</sub> caused by suitable energy band alignment, *Adv. Funct. Mater.* 25 (2015) 3074–3080.
- [37] H.J. Cheng, J.G. Hou, O. Takeda, X.M. Guo, H.M. Zhu, A unique Z-scheme 2D/2D nanosheet heterojunction design to harness charge transfer for photocatalysis, *J. Mater. Chem. A* 3 (2015) 11006–11013.
- [38] H. Kim, O. Renault, A. Tyurnina, J.-P. Simonato, D. Rouchon, D. Mariolle, N. Chevalier, J. Dijon, Doping efficiency of single and randomly stacked bilayer graphene by iodine adsorption, *Appl. Phys. Lett.* 105 (2014) 011605.